

Article

Microcystis@TiO₂ Nanoparticles for Photocatalytic Reduction Reactions: Nitrogen Fixation and Hydrogen Evolution

Xuan Li ^{1,2}, Jingcai Chang ^{1,*}, Shijie Zhang ^{1,2}, Lihui Xiao ^{1,2}, Xiaoge Wu ^{3,*} and Zuoli He ^{1,2,*} 

¹ Shandong Key Laboratory of Water Pollution Control and Resource Reuse, School of Environmental Science and Engineering, Shandong University, Qingdao 266237, China; 202012951@mail.sdu.edu.cn (X.L.); 201912711@mail.sdu.edu.cn (S.Z.); 201922210085@mail.sdu.edu.cn (L.X.)

² Suzhou Research Institute, Shandong University, Suzhou 215123, China

³ School of Environmental Science and Engineering, Yangzhou University, Yangzhou 225000, China

* Correspondence: changjingcai@sdu.edu.cn (J.C.); xgwu@yzu.edu.cn (X.W.); zlhe@sdu.edu.cn (Z.H.)

Abstract: Solar-driven photocatalysis has been known as one of the most potential technologies to tackle the energy shortage and environmental pollution issues. Utilizing bio-pollutants to prepare functional materials has been considered as a green option. Herein, we used *Microcystis aeruginosa* as a bio-template to fabricate a *Microcystis*@TiO₂ photocatalyst using a calcination method. The as-prepared *Microcystis*@TiO₂ showed prominent ability as well as favorable stability for photocatalytic reduction reactions including hydrogen evolution and nitrogen fixation. Under light illumination, *Microcystis*@TiO₂ calcined at 550 °C exhibited optimal photo-reduced activity among all samples, with the highest hydrogen evolution (1.36 mmol·g⁻¹·h⁻¹) and ammonia generation rates (0.97 mmol·g⁻¹·h⁻¹). This work provides a feasible approach to prepare functional materials from disposed pollutants.

Keywords: photocatalyst; TiO₂; *Microcystis*; H₂ production; N₂ fixation



Citation: Li, X.; Chang, J.; Zhang, S.; Xiao, L.; Wu, X.; He, Z.

Microcystis@TiO₂ Nanoparticles for Photocatalytic Reduction Reactions: Nitrogen Fixation and Hydrogen Evolution. *Catalysts* **2021**, *11*, 1443. <https://doi.org/10.3390/catal11121443>

Academic Editors: Wonyong Choi, Detlef W. Bahnemann, Ioannis Konstantinou, Ewa Kowalska, Magdalena Janus, Vincenzo Vaiano and Zhi Jiang

Received: 11 November 2021
Accepted: 24 November 2021
Published: 26 November 2021

Publisher's Note: MDPI stays neutral with regard to jurisdictional claims in published maps and institutional affiliations.



Copyright: © 2021 by the authors. Licensee MDPI, Basel, Switzerland. This article is an open access article distributed under the terms and conditions of the Creative Commons Attribution (CC BY) license (<https://creativecommons.org/licenses/by/4.0/>).

1. Introduction

Fast-growing industry worldwide is leading to environmental pollution and energy shortage, which are global problems that urgently need to be addressed. Therefore, the demand for green and clean sources has been increasing rapidly. As the primary sources for meeting the ever-increasing demand, hydrogen, and ammonia have attracted extensive attention [1–6]. However, traditional production processes not only consume a huge amount energy but also cause a series of environmental problems [7–11]. For example, at the current stage, the industrial synthesis of ammonia is accomplished by the Haber-Bosch process [12,13]. The Haber-Bosch preparation process requires extreme reaction conditions, i.e., high temperature (400–600 °C) and high pressure (20–40 MPa), and consumes vast fossil fuels as well as releasing a huge amount of CO₂ gas (≥1.6% of total global CO₂ emissions). In recent decades, much effort has been expended in finding effective techniques to solve the above problems.

Solar-driven photocatalysis, which is economical, sustainable, and environmentally friendly, has captured extensive attention [14–18]. Photocatalytic reduction reactions (such as hydrogen evolution, nitrogen fixation, and carbon dioxide reduction) can often store the solar energy into chemical energy [19–25]. As one of the most widely studied photosensitive materials, Titanium dioxide (TiO₂) is of great concern in the research of photocatalysis [26–34]. Several decades of research have proven the outstanding properties of TiO₂ in photocatalysis, such as low cost, non-toxicity, and excellent stability. Moreover, TiO₂ is a suitable semiconductor material for photocatalytic reduction reactions. Recently, Yu et al. reported that the successful preparation of Z-scheme TiO₂/Au/BiOI nanocomposite exhibited excellent photocatalytic performance for N₂ photo-fixation with a fixation

rate of $543.53 \mu\text{mol L}^{-1} \text{h}^{-1} \text{g}^{-1}$ [35]. Ding et al. showed that by using N-TiO₂/Ti₃C₂ composites, photocatalytic pollutant degradation and nitrogen fixation performance could be promoted enormously [36]. Lan et al. introduced 2-ethylimidazole to synthesize a type of ordered mesoporous TiO₂, which enhanced the generation rate of H₂ [37]. Besides, Xu et al. fabricated S-scheme TiO₂/CsPbBr₃ heterojunction photocatalysts through an electrostatic assembly method to boost photocatalytic CO₂ reduction [38]. Although some progress has been made in improving the photocatalytic ability of TiO₂-based photocatalysts, compared with the industrial process, the photocatalytic yield still needs to be promoted.

In recent years, the increasing energy demand has not only impelled us to use green energies more reasonably but also to store clean renewable resources into chemical products or fuels. Utilizing pollutants to prepare functional materials has been attracting considerable attention. *Microcystis aeruginosa* is one of the predominant organisms responsible for causing harmful algal blooms [39–41]. *Microcystis aeruginosa* is well known to produce toxins [42]. The toxins released from *Microcystis* cells are commonly observed in surface water and threatens the drinkability of reservoir water, as it is harmful to the environment and humans [39]. The utilization of *Microcystis* cells can change the current situation of high-cost treatment [36,38–40], and could maybe even create a platform with high potential to produce cost-competitive products. In the past few years, many techniques have been applied to solve the issue, such as physical treatments, chemical treatments, and biological treatments [41,43,44]. However, it is difficult to completely control *Microcystis* and prevent HABs in one treatment due to each treatment having its characteristic advantages and disadvantages. For instance, physical and chemical measures can remove *Microcystis* efficiently, but also result in resource waste and secondary pollution [43]. Biological treatment seems to use natural processes to realize the decomposition of organic substances, but in fact, it is a complex, long-term process, and will introduce a *Resistance Gene* sometime [45].

Herein, as an attempt to utilize pollutants as resources, we used *Microcystis* cells as one of the raw materials to fabricate TiO₂-based functional materials (*Microcystis*@TiO₂) via a calcination technique at different temperatures. The preparation process not only utilized pollutants-harmful algae as bio-template but also converted them to value-added products. The structures and properties of *Microcystis*@TiO₂ were investigated by all sorts of characterization methods such as X-ray powder diffraction (XRD), X-ray photoelectron spectroscopy (XPS), and UV–vis diffuse reflectance spectra (UV–vis DRS). The photocatalytic reduction activities of the photocatalyst was tested by nitrogen fixation and hydrogen generation. The possible reduction mechanism was also proposed.

2. Results and Discussion

2.1. Characterization of Photocatalysts

TiO₂ has three different polymorphic phases: the rutile phase, anatase phase, and brookite phase. The rutile phase is the most thermodynamically stable phase among these three natural phases of TiO₂. The applications of the rutile phase is wide, because of its unusual properties, such as high optical, high chemical stability, high dielectric constant, and good scattering efficiency. The schematic preparation process of the samples is displayed in Figure 1. *Microcystis* solution was dispersed in 80 mL deionized water under ice bath and the pH of the solution was adjusted to 4.0. After stirring for 30 min, 2 mL 1 mol/L tetra butyl titanate (TiCl₄) was added slowly under an ice bath and stirred for 24 h at room temperature. Then, the mixture was heated at 70 °C and kept stirring for 2 h. The yellow-white precipitate was collected and dried at 60 °C overnight. Finally, the obtained product was calcined in a muffle furnace to remove *Microcystis aeruginosa* and make proper carbon doping. The structure and morphology of the obtained samples were analyzed by using X-ray diffraction (XRD), scanning electron microscopy (SEM), and transmission electron microscopy (TEM). Figure 2 shows the XRD patterns of the samples. The patterns of the samples calcined under different temperatures matched well with the rutile phase (JCPDS no. 21–1276). The peaks around 27.4°, 36.1°, 41.2°, 54.3°, 56.6°, and 69.0° corresponded to the (110), (101), (111), (211), (220), and (301) crystal planes of rutile TiO₂, respectively.

The *Microcystis*@TiO₂-400 exhibited weak XRD peaks, which related to its low crystallinity. With the rise of calcination temperature, the diffraction intensity increased and the crystal characteristics of rutile TiO₂ became more defined. Figures 3 and 4 are the SEM and TEM images that were used to analyze the morphology of the samples. As depicted in Supplementary Materials Figure S1, the sample without calcination was surrounded by many spheroidal particles. After calcination, the morphology of the spheroidal particles was greatly different, as the thin rutile rods were in-situ grown on the surface during the calcination process. As shown in Figure 3a–d, the *Microcystis*@TiO₂-550 possesses a sea urchin-like morphology with a diameter of about 5 μm. When calcined at 800 °C, the end of the nano rod became sharper, indicating that the crystalline increased.

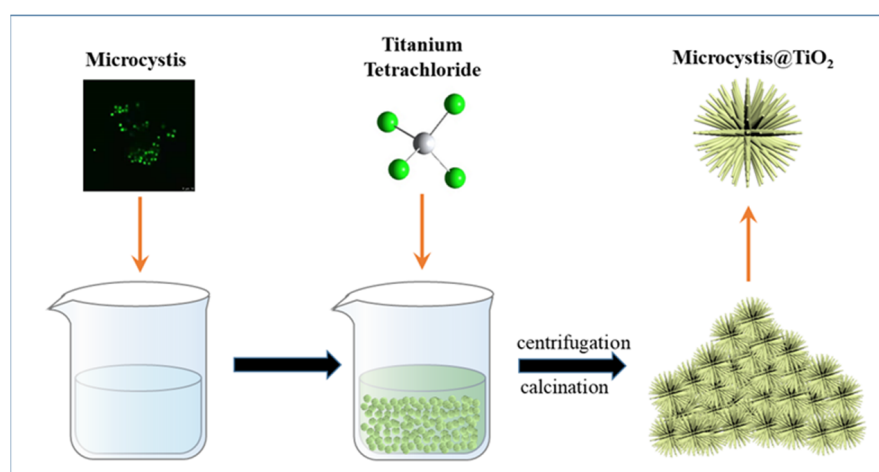


Figure 1. The synthetic process of *Microcystis*@TiO₂.

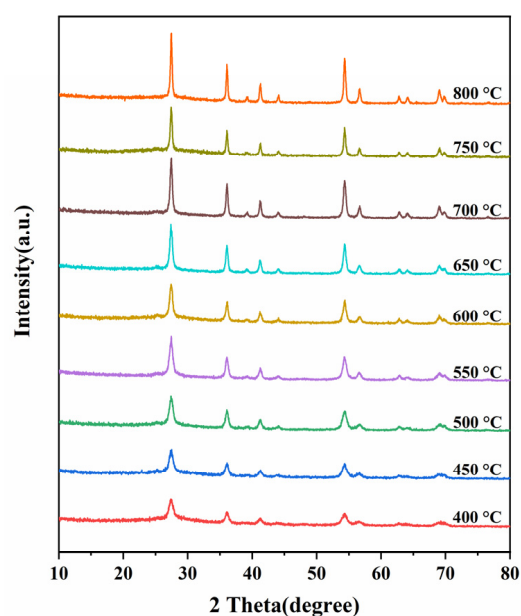


Figure 2. XRD spectra for *Microcystis*@TiO₂ under different calcination temperatures.

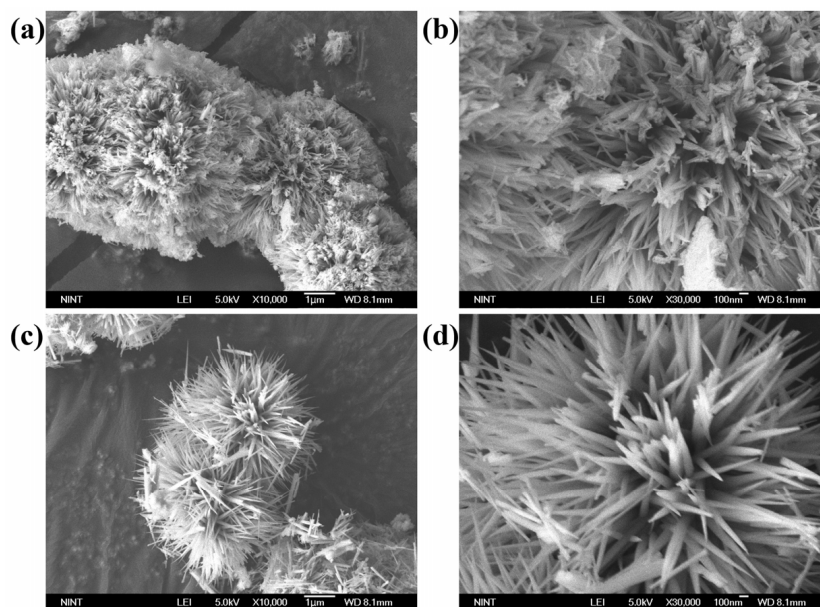


Figure 3. SEM images of (a–d) *Microcystis*@TiO₂-550.

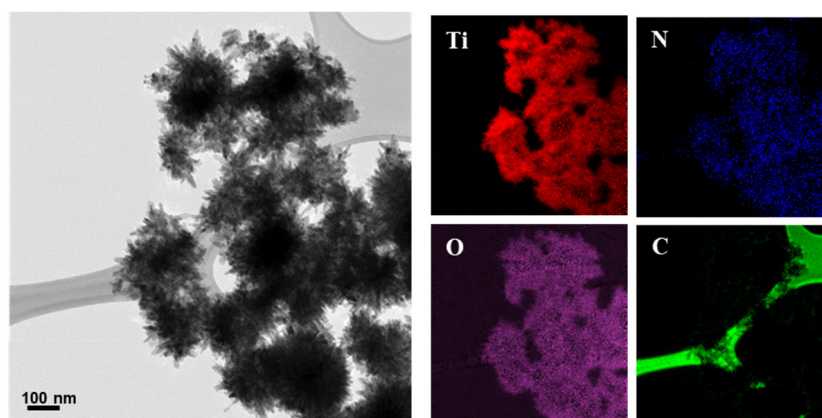


Figure 4. The elements mapping data of *Microcystis*@TiO₂-550.

This morphology can also be observed in TEM images. These results indicate that the sea urchin structure was fabricated by the direct growth of the surface of the bio-templates, which were removed at high temperatures. The *Microcystis*@TiO₂-550 was selected as the representative samples for TEM measurement, owing to its excellent photocatalytic performance. The TEM images of *Microcystis*@TiO₂-550 were displayed in Figure 5. The nanorods were grown on the surface, which cohered with SEM investigation. As shown in Supplementary Materials Figure S2, the *Microcystis*@TiO₂-550 shows the clear lattice fringes with the lattice distances of 0.14, 0.20, and 0.25 nm, matching well with the (221), (210), and (101) facets of rutile TiO₂, respectively. The results agree with the XRD pattern depicted in Figure 2. The results further indicate that the *Microcystis* successfully worked as a bio-template. As presented in Figure 4, elements mapping data are uniformly distributed in the *Microcystis*@TiO₂-550 composites, which verify the elemental composition of the sample.

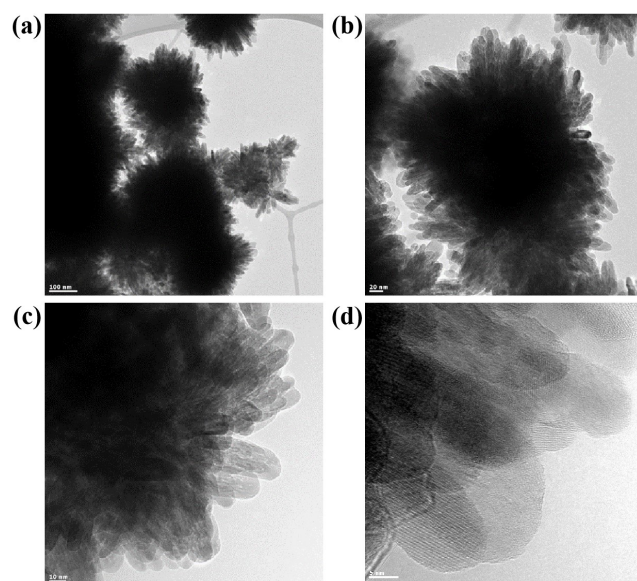


Figure 5. The TEM image of (a–d) *Microcystis@TiO₂-550*.

The porous structure and surface area of *Microcystis@TiO₂-550* composites were investigated by N₂-adsorption measurements, the nitrogen adsorption-desorption isotherms of the prepared samples were presented in Supplementary Materials Figure S3. The N₂ adsorption isotherms of the samples possess representative type-III with a hysteresis loop, demonstrating the existence of a highly porous structure. The Brunauer–Emmett–Teller (BET) surface area of the *Microcystis@TiO₂-400*, *Microcystis@TiO₂-550*, and *Microcystis@TiO₂-800* were 42, 27, and 12 m²/g. It is seen that the surface area decreases with the increasing calcination temperatures. Such phenomena are attributed to the removal of *Microcystis* and high crystalline.

UV–Vis diffuse reflectance spectra (UV–Vis DRS) was conducted to investigate the optical properties. As shown in Figure 6, all samples had an obvious absorption band in the ultraviolet region. *Microcystis@TiO₂-550* processes an increased absorption capability in the visible region compared with other samples, which is related to the carbon introduced from *Microcystis*. The *Microcystis@TiO₂-550* and *Microcystis@TiO₂-800* were selected as the representative samples for calculating the optical bandgap. According to the Kubelka–Munk function vs. light energy shown in Supplementary Materials Figure S4 in supporting information, the bandgap energy of *Microcystis@TiO₂-550* was calculated to be 2.91 eV, which was smaller than that of *Microcystis@TiO₂-800* (3.0 eV). The smaller bandgap could be attributed to the progress of calcination, which caused the different quantities of element doping, especially carbon-doping.

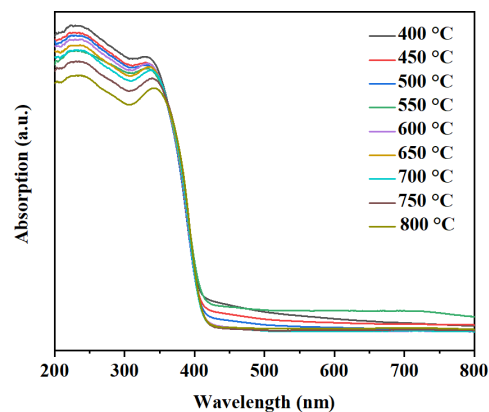


Figure 6. UV–vis diffuse reflectance spectra (UV–vis DRS) of the prepared *Microcystis@TiO₂*.

The XPS survey spectra were carried out to test the binding energy of the element of the *Microcystis@TiO₂*. The survey spectra in Figure 7a demonstrated the existence of Ti, C, and O elements. The high-resolution Ti 2p XPS spectrum was shown in Figure 7b, the peaks at 459.20 eV and 464.95 eV in Ti 2p can be ascribed to the Ti⁴⁺ state [46]. Compared with the sample without calcination, the peaks of *Microcystis@TiO₂*-550 showed a shift to higher binding energy and revealed the changes in the chemical environment of Ti atoms (Supplementary Materials Figure S5). As shown in Figure 7c, the O 1s spectrum for *Microcystis@TiO₂* shows two peaks at 530.45 eV and 530.00 eV, which can be indexed to the O²⁻ in the lattice of *TiO₂* as well as the surface adsorbed hydroxyl group, respectively [47]. The peak around 531.55 eV is assigned to the oxygen vacancy on the *TiO₂* surface. The C 1s XPS spectrum for *Microcystis@TiO₂*-550 shows three characteristic peaks. Typically, the peaks located at 285.0 eV and 286.5 eV can be ascribed to C=C and C–O, respectively. The peak at 288.8 eV is assigned to O–C=O functional groups [48]. It is noted that the peak around 285.0 eV for C=C bond is owed to the amorphous carbon from *Microcystis* left in *Microcystis@TiO₂*-550 [49].

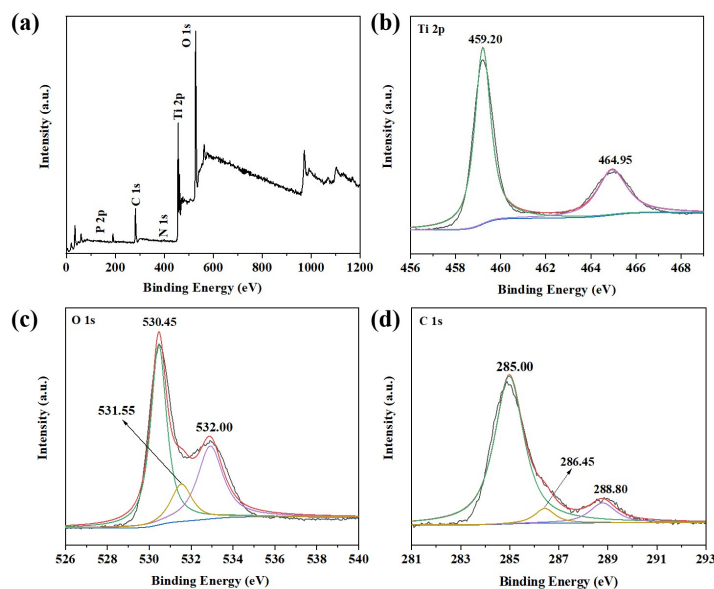


Figure 7. (a) XPS spectra of *Microcystis@TiO₂*-550 and the corresponding high-resolution spectra of (b) Ti 2p, (c) O 1s, (d) C 1s.

2.2. Photocatalytic Activity

2.2.1. Photocatalytic Nitrogen Fixation Performance of *Microcystis@TiO₂* Composites

The photocatalytic nitrogen fixation performance of the composites under different calcination temperatures was shown in Figure 8. To confirm that the NH₃ originated from the photocatalytic nitrogen fixation (rather than some other nitrogen source), all samples had been conducted by using Ar instead of N₂ to eliminate interference. The produced ammonia was determined by spectrophotometrically measuring with the Nessler's reagent. As displayed in Figure 8a, the activities for nitrogen fixation followed the order: *Microcystis@TiO₂*-550 > *Microcystis@TiO₂*-400 > *Microcystis@TiO₂*-450 > *Microcystis@TiO₂*-500 > *Microcystis@TiO₂*-600 > *Microcystis@TiO₂*-650 > *Microcystis@TiO₂*-700 > *Microcystis@TiO₂*-750 > *Microcystis@TiO₂*-800. The *Microcystis@TiO₂*-550 sample exhibited the best photocatalytic nitrogen fixation performance (0.97 mmol·g⁻¹·h⁻¹) compared with other samples. The nitrogen fixation rate of *Microcystis@TiO₂*-550 was 1.9 times higher than that of *Microcystis@TiO₂*-800. It is noted that the sample without calcination showed the lowest ability for ammonia generation (0.001 mmol·g⁻¹·h⁻¹), which may be related to the lower catalysts amount in the composite. Therefore, the NH₃ generation rate of the samples increased a lot after calcination. As Figure S6 in Supplementary Materials showed, the blank test indicated that there was no NH₃ produced in the absence of light and a photocatalyst.

By the way, the *Microcystis*@TiO₂-550 photocatalyst also exhibited excellent stability see Figure 8b. After three cycles, no noticeable decrease of photocatalytic nitrogen fixation was observed. In addition, we found that the samples exhibited higher photocatalytic nitrogen fixation performance under weak acid conditions compared with other conditions (Figure S7 in Supplementary Materials).

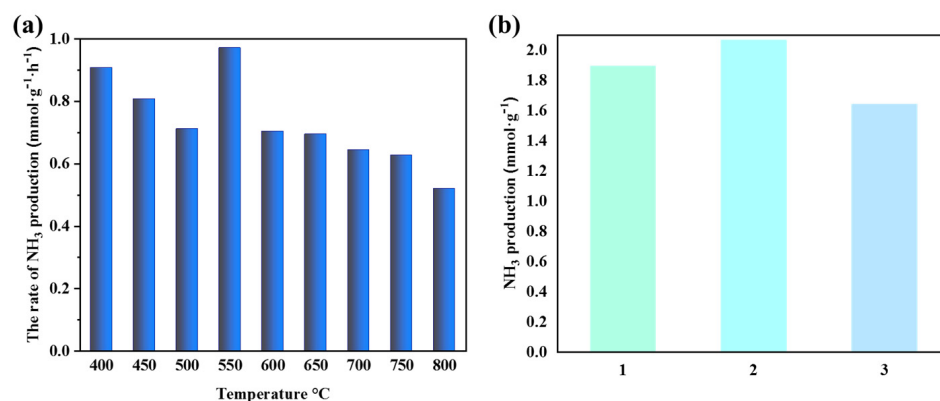


Figure 8. (a) The rate of NH₃ evolution with 2 h of illumination over the prepared *Microcystis*@TiO₂. (b) The stability of photocatalytic NH₃ production over *Microcystis*@TiO₂-550.

2.2.2. Photocatalytic Hydrogen Generation Performance of *Microcystis*@TiO₂ Composites

The photocatalytic hydrogen generation performance was assessed by using a Xe lamp in a Pyrex reactor for H₂ production as well as methanol as an electron donor. The results are presented in Figure 9. With the prolongation of the irradiation time, a linear increase of H₂ amount can be observed in the *Microcystis*@TiO₂ samples (Figure S8 in the Supplementary Materials). With the increase in calcination temperature from 400 to 500 °C, the rate of hydrogen evolution decreased. When the calcination temperature continuously increased to 550 °C, the hydrogen evolution rate reached a maximum. However, the rate of hydrogen evolution continuously decreased, with a further rise in the calcination temperature from 550 to 800 °C. The hydrogen generation rate is 1.36 mmol·g⁻¹·h⁻¹, which was three times higher than that of *Microcystis*@TiO₂-800 sample. The *Microcystis*@TiO₂-550 showed the optimal photocatalytic activity, indicating that the carbon doping was the key factor affecting the photocatalytic activities. The stability of the *Microcystis*@TiO₂-550 for hydrogen production was also evaluated and the results were displayed in Figure 9b. After three-time cycling reaction operation, there was no noticeable decrease of photocatalytic H₂ evolution, which indicated good photocatalytic stability of *Microcystis*@TiO₂ composites. It is attributed to *Microcystis*@TiO₂ photocatalysts with active exposed surfaces, voids, which provide more catalytic active sites to promote photocatalytic hydrogen production by accelerating the charge transfer. In summary, the reusable characteristic of *Microcystis*@TiO₂ possessed potential value for photocatalytic reduction applications, such as H₂ production and nitrogen fixation.

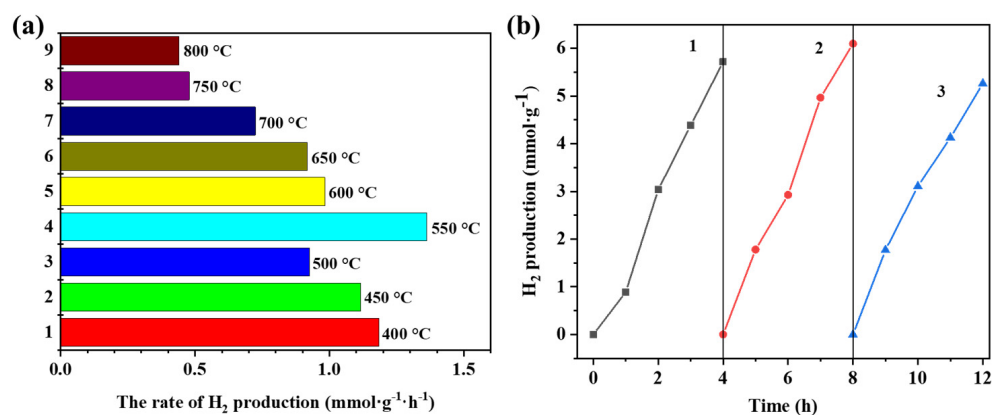


Figure 9. (a) The rate of H₂ evolution with 4 h of illumination over the prepared *Microcystis@TiO₂*. (b) The stability of photocatalytic H₂ evolution over *Microcystis@TiO₂-550*.

2.3. Photoelectrochemical Properties

The photoelectrochemical (PEC) analysis was implemented to evaluate the charge transfer and separation behaviors of the samples. In this work, we selected three samples, *Microcystis@TiO₂-400*, *Microcystis@TiO₂-550*, and *Microcystis@TiO₂-800*, as representatives. The photocurrent-time curves consisted of three similar cycles during the repeated chopped-light irradiation, and the rising curve corresponded to the light irradiation of each cycle. When the light is turned on, the surface photocurrents of the samples reached a value. When the light is turned off, the photocurrent no generation was observed in the photocurrent. Under illumination, the photogenerated charge carriers in a photocatalyst-coated electrode migrated through a series of particle boundaries to reach the FTO substrate to be reflected as the IT spectra. Thereby, the intensity of the photocurrent was mainly dominated by the number of charge carriers that transferred to the FTO substrate, and the defect and active sites could trap electrons as electron reservoirs during their transfer, reducing the photocurrent [25]. As displayed in Figure 10a, the average photo-current density of *Microcystis@TiO₂-400*, *Microcystis@TiO₂-550*, and *Microcystis@TiO₂-800* were calculated to be ~0.006, ~0.012, and ~0.004 $\mu\text{A}/\text{cm}^2$, respectively. It is indicated that *Microcystis@TiO₂-550* is an effective photogenerated separation carrier in these three samples. Additionally, the slow decreasing photocurrent of *Microcystis@TiO₂-550* under irradiation implies the more defect and active sites in this sample. As a result, the modified photocatalyst may provide excellent optical absorption of light and effective separation of the photogenerated carriers. This also supports the previous statement that appropriate carbon doping is more conducive to the separation and transfer of charge carriers. Electrochemical impedance spectra (EIS) were also measured to explore the charge carrier transport behaviors. As displayed in Figure 10b, as compared to the *Microcystis@TiO₂-400* and *Microcystis@TiO₂-800*, the *Microcystis@TiO₂-550* exhibited a smaller impedance arc radius in the Nyquist plots. This result demonstrated that the *Microcystis@TiO₂-550* possessed the slightest interfacial resistance, which is beneficial for faster charge transfer, which was consistent with the test results of the transient photocurrent response.

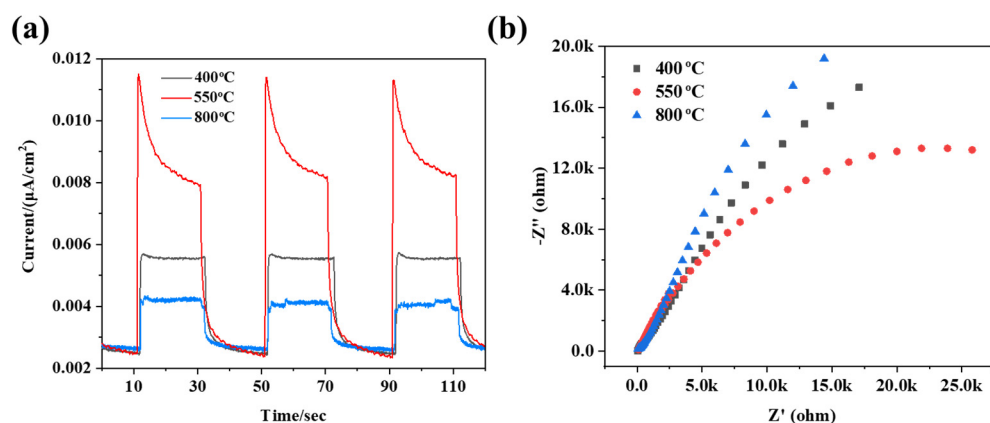


Figure 10. (a) Transient photocurrent responses and (b) EIS Nyquist plots of *Microcystis@TiO₂-400*, *Microcystis@TiO₂-550* and *Microcystis@TiO₂-800*.

2.4. Mechanism

Based on the above experiment results, a possible photocatalytic mechanism for *Microcystis@TiO₂* photocatalyst was proposed in Figure 11, indicating the charge separation and transfer pathway. *Microcystis@TiO₂* calcined at 550 °C showed highly efficient photocatalytic reduction performances, which is related to the unique structures from *Microcystis* cells and proper carbon doping. Under irradiation, the photogenerated electrons of the *Microcystis@TiO₂* in the valence band (VB) will be excited to the conduction band (CB) and the holes are left in the VB. Then, the photogenerated electrons in the CB will be transferred to the Pt surface and combined with H⁺ to generate H₂ (N₂ fixation to NH₃). Meanwhile, the carbon doping introduces a defect energy level, which could capture the photogenerated carriers and enhance the charge separation. In addition, the sea urchin-like structure resulting from *Microcystis aeruginosa* enables a high surface area and the proper carbon doping enables more defects and active sites, which are beneficial for the photocatalytic reduction process.

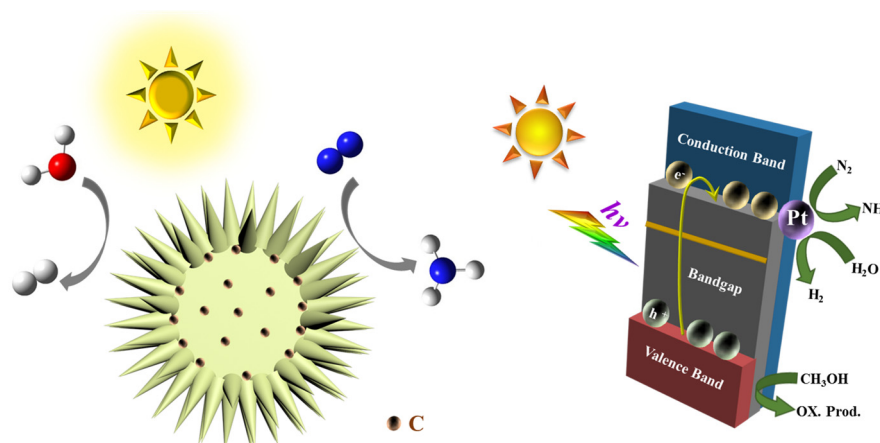


Figure 11. Schematic illustration for the photocatalytic mechanism over *Microcystis@TiO₂*.

3. Materials and Methods

3.1. Synthesis of *Microcystis@TiO₂* Composites

Five mL 10⁷ cells/mL *Microcystis* solution was washed by phosphate buffer saline three times. The above solution was dispersed in 80 mL deionized water in an ice bath for 30 min and the pH of the solution was adjusted to 4.0. 2 mL tetrabutyl titanate (TiCl₄) with a concentration of 1 mol/L being added and slowly stirred for 24 h at room temperature. The mixture was heated to 70 °C and stirring was maintained for 2 h. The yellow-white precipitate was collected and dried at 60 °C overnight. Finally, the product was transferred

into a muffle furnace and calcined at different temperatures (400 °C, 450 °C, 500 °C, 550 °C, 600 °C, 650 °C, 700 °C, 750 °C, and 800 °C) for 2 h to remove *Microcystis* cells and make proper carbon doping. The obtained *Microcystis*@TiO₂ composites were named *Microcystis*@TiO₂-400, *Microcystis*@TiO₂-450, *Microcystis*@TiO₂-500, *Microcystis*@TiO₂-550, *Microcystis*@TiO₂-600, *Microcystis*@TiO₂-650, *Microcystis*@TiO₂-700, *Microcystis*@TiO₂-750, and *Microcystis*@TiO₂-800, respectively.

3.2. Characterization

X-ray powder diffraction (XRD) of the samples were carried out at an X-ray diffractometer (XRD, Rigaku, RINT 2000, Tokyo, Japan). Scanning electron microscopy (SEM, FEI, Quanta 250 FEG, Boston, MA, USA) and transmission electron microscopy (TEM, JEOL, JEM-2100FS, Tokyo, Japan) were performed to investigate the morphology and microstructures of the samples. X-ray photoelectron spectroscopy (XPS, PHI 5000 VersaProbe II, Tokyo, Japan) analyses were carried out on ESCALAB spectrometer with a monochromatic Al-K α (1486.6 eV) as X-ray source. The UV–vis absorption spectra of the samples were obtained from a UV–vis spectrophotometer (UV-2600, Shimadzu, Kyoto, Japan) with BaSO₄ as the reference, and UV–vis spectra were recorded within a wavelength range from 200 to 800 nm. Brunauer-Emmett-Teller (BET) experiments were collected on an ASAP2460 Surface Area.

3.3. Photocatalytic Nitrogen Fixation

The photocatalytic nitrogen fixation activity tests were performed in a Pyrex irradiation reactor (57 mL). In a typical test, 20 mg photocatalyst powder was dispersed into a CH₃OH aqueous solution (36 mL of deionized water + 4 mL of CH₃OH). Then, moderate H₂PtCl₆ was placed into the above solution. The light source used was a 300 W Xe lamp (Perfect Light, PLS-SXE300, Beijing, China). Before switching on the light, N₂ was bubbled through at a flow rate of 20 mL min⁻¹ and the reaction solution was stirred for 30 min in the dark. After irradiation for 2 h, 5 mL of the reaction solution was collected, and the photocatalyst was removed through syringe filters. The ammonia concentration was detected by the Nesslerization method. All samples were performed by using Ar as a nitrogen source instead of N₂ to eliminate interference.

3.4. Photocatalytic Hydrogen Evolution

The photocatalytic H₂ evolution activity tests were conducted in a Pyrex irradiation reactor (57 mL) with a closed cycle gas circulation system connected to a gas chromatography instrument (Shimadzu; GC-8A, MS-5A column, TCD, argon carrier, Kyoto, Japan). Typically, 20 mg photocatalyst powder was dispersed into a methanol (CH₃OH) aqueous solution (36 mL of deionized water + 4 mL of CH₃OH) and the pH of the solution was adjusted to 4.0. Then, moderate H₂PtCl₆ was placed into the above solution. Before irradiation, the air in the reactor was degassed and replaced with Ar gas. A 300 W Xe lamp (Perfect Light, PLS-SXE300) was used as the incident light source. The gas produced in the reaction was detected by using gas chromatography (GC, HP6890A) equipped with a thermal conductivity detector (TCD) with Ar as carrier gases.

3.5. Photoelectrochemical Measurements

In the photoelectrochemical analysis of the prepared samples, including the electrical impedance spectroscopy (EIS), transient photocurrent responses were tested using a standard three-electrode cell on the CHI 660E electrochemical workstation, where the Pt foil was the counter electrode, photocatalyst-coated FTO substrate (1 × 1 cm²) was the working electrode, and Ag/AgCl was the reference electrode. A 300 W Xe lamp (Perfect Light, PLS-SXE300) was employed as the light source, which was the same as the photocatalytic process.

4. Conclusions

In general, single *Microcystis* cells were utilized as a bio-template to prepare *Microcystis@TiO₂* photocatalysts by a calcination method. The *Microcystis@TiO₂* possessed excellent photocatalytic reduction performance in hydrogen evolution and nitrogen fixation. Among all the samples, *Microcystis@TiO₂* calcined at 550 °C shows highly efficient photocatalytic reduction performances, which is related to the unique structures from *Microcystis* and proper carbon doping. Within 2 h of irradiation, the ammonia generation from nitrogen fixation of *Microcystis@TiO₂*-550 reached 0.97 mmol·g⁻¹·h⁻¹. The hydrogen generation rate of *Microcystis@TiO₂*-550 reached 1.36 mmol·g⁻¹·h⁻¹. The *Microcystis@TiO₂*-550 exhibited good stability in successive photocatalytic hydrogen generation and nitrogen fixation process. This work provided an approach that not only utilizes pollutants but also transforms them into functional materials. It is expected that these functional materials with excellent photocatalytic performance could be widely used in solar energy conversion.

Supplementary Materials: The following are available online at <https://www.mdpi.com/article/10.3390/catal11121443/s1>, Figure S1: The SEM image of the *Microcystis@TiO₂* sample without calcination, Figure S2: The TEM image of *Microcystis@TiO₂*-550, Figure S3: The nitrogen adsorption-desorption isotherms of *Microcystis@TiO₂* samples, Figure S4: The Kubelka-Munk function vs. light energy of *Microcystis@TiO₂* samples, Figure S5: The Ti 2p high-resolution spectra of samples without calcination (top) and *Microcystis@TiO₂*-550 (down), Figure S6: The production of NH₃ in absence of photocatalyst and light irradiation, Figure S7: The rate of NH₃ production under different pH conditions, Figure S8: The production of H₂ under 4h illumination.

Author Contributions: Conceptualization, X.W. and Z.H.; methodology, X.L.; validation, X.L., S.Z. and L.X.; investigation, L.X.; resources, J.C. and Z.H.; data curation, X.L.; writing—original draft preparation, X.L. and Z.H.; writing—review and editing, J.C., X.W. and Z.H.; supervision, X.W. and Z.H.; project administration, X.W. and Z.H.; funding acquisition, Z.H. All authors have read and agreed to the published version of the manuscript.

Funding: This research was supported under the framework of the Natural Science Foundation of Jiangsu Province (No. BK20200237), the Young Taishan Scholars Program of Shandong Province (No. tsqn. 201909026), Youth Interdisciplinary Science and Innovative Research Groups of Shandong University (Grant No. 2020QNQT014), and the Key Laboratory of Organic Compound Pollution Control Engineering (MOE) Foundation (No. 20190202).

Institutional Review Board Statement: Not applicable.

Informed Consent Statement: Not applicable.

Data Availability Statement: Data is contained within the article.

Acknowledgments: The authors thank S. Wang from The State Key Laboratory of Microbial Technology, Shandong University for his assistance with SEM. The authors would like to thank Conghua Qi from Shiyanjia Lab (<http://www.shiyanjia.com>) for the TEM and XPS analysis.

Conflicts of Interest: The authors declare no conflict of interest.

References

1. Xiang, Q.; Li, F.; Zhang, D.; Liao, Y.; Zhou, H. Plasma-based surface modification of g-C₃N₄ nanosheets for highly efficient photocatalytic hydrogen evolution. *Appl. Surf. Sci.* **2019**, *495*, 143520. [[CrossRef](#)]
2. Xiang, Q.; Cheng, F.; Lang, D. Hierarchical layered WS₂/graphene-modified CdS nanorods for efficient photocatalytic hydrogen evolution. *Chemosuschem* **2016**, *9*, 996–1002. [[CrossRef](#)]
3. Xiang, Q.; Yu, J. Graphene-based photocatalysts for hydrogen generation. *J. Phys. Chem. Lett.* **2013**, *4*, 753–759. [[CrossRef](#)]
4. Cheng, L.; Li, X.; Zhang, H.; Xiang, Q. Two-dimensional transition metal MXene-based photocatalysts for solar fuel generation. *J. Phys. Chem. Lett.* **2019**, *10*, 3488–3494. [[CrossRef](#)]
5. Shen, R.; Ren, D.; Ding, Y.; Guan, Y.; Ng, Y.H.; Zhang, P.; Li, X. Nanostructured CdS for efficient photocatalytic H₂ evolution: A review. *Sci. China Mater.* **2020**, *63*, 2153–2188. [[CrossRef](#)]
6. Xiao, L.; Li, X.; Zhang, J.; He, Z. MgB₄ MXene-like nanosheets for photocatalytic hydrogen evolution. *ACS Appl. Nano Mater.* **2021**, *4*, 12779–12787. [[CrossRef](#)]

7. Jiang, Z.; Chen, Q.; Zheng, Q.; Shen, R.; Zhang, P.; Li, X. Constructing 1D/2D schottky-based heterojunctions between $\text{Mn}_{0.2}\text{Cd}_{0.8}\text{S}$ nanorods and Ti_3C_2 nanosheets for boosted photocatalytic H_2 evolution. *Acta Phys.-Chim. Sin.* **2021**, *37*, 2010059.
8. Wageh, S.; Al-Ghamdi, A.A.; Jafer, R.; Li, X.; Zhang, P. A new heterojunction in photocatalysis: S-scheme heterojunction. *Chin. J. Catal.* **2021**, *42*, 667–669. [[CrossRef](#)]
9. Shen, R.; Ding, Y.; Li, S.; Zhang, P.; Xiang, Q.; Ng, Y.H.; Li, X. Constructing low-cost Ni_3C /twin-crystal $\text{Zn}_{0.5}\text{Cd}_{0.5}\text{S}$ heterojunction/homojunction nanohybrids for efficient photocatalytic H_2 evolution. *Chin. J. Catal.* **2021**, *42*, 25–36. [[CrossRef](#)]
10. He, Z.; Zhang, J.; Li, X.; Guan, S.; Dai, M.; Wang, S. 1D/2D Heterostructured photocatalysts: From design and unique properties to their environmental applications. *Small* **2020**, *16*, 2005051. [[CrossRef](#)] [[PubMed](#)]
11. Zhang, S.J.; He, Z.L.; Xu, S.S.; Li, X.; Zhang, J.; Zhan, X.P.; Dai, M.; Wang, S.G. In situ liquid-phase growth strategies of g- C_3N_4 solar-driven heterogeneous catalysts for environmental applications. *Sol. RRL* **2021**, *5*, 2100233. [[CrossRef](#)]
12. Shi, R.; Zhang, X.; Waterhouse, G.I.N.; Zhao, Y.; Zhang, T. The journey toward low temperature, low pressure catalytic nitrogen fixation. *Adv. Energy Mater.* **2020**, *10*, 2000659. [[CrossRef](#)]
13. Wang, S.Y.; Ichihara, F.; Pang, H.; Chen, H.; Ye, J.H. Nitrogen fixation reaction derived from nanostructured catalytic materials. *Adv. Funct. Mater.* **2018**, *28*, 1803309. [[CrossRef](#)]
14. Shen, R.; Lu, X.; Zheng, Q.; Chen, Q.; Ng, Y.H.; Zhang, P.; Li, X. Tracking S-scheme charge transfer pathways in $\text{Mo}_2\text{C}/\text{CdS}$ H_2 evolution photocatalysts. *Sol. RRL* **2021**, *5*, 2100177. [[CrossRef](#)]
15. Lan, Z.A.; Ren, W.; Chen, X.; Zhang, Y.; Wang, X. Conjugated donor-acceptor polymer photocatalysts with electron-output ldquotentaclesrdquo for efficient hydrogen evolution. *Appl. Catal. B* **2019**, *245*, 596–603. [[CrossRef](#)]
16. Lin, L.; Lin, Z.; Zhang, J.; Cai, X.; Lin, W.; Yu, Z.; Wang, X. Molecular-level insights on the reactive facet of carbon nitride single crystals photocatalysing overall water splitting. *Nat. Catal.* **2020**, *3*, 649–655. [[CrossRef](#)]
17. Cheng, L.; Zhang, D.; Liao, Y.; Li, F.; Zhang, H.; Xiang, Q. Constructing functionalized plasmonic gold/titanium dioxide nanosheets with small gold nanoparticles for efficient photocatalytic hydrogen evolution. *J. Colloid Interface Sci.* **2019**, *555*, 94–103. [[CrossRef](#)]
18. Li, Y.; Gong, F.; Zhou, Q.; Feng, X.; Fan, J.; Xiang, Q. Crystalline isotype heptazine-/triazine-based carbon nitride heterojunctions for an improved hydrogen evolution. *Appl. Catal. B* **2020**, *268*, 118381. [[CrossRef](#)]
19. Yu, J.; Low, J.; Xiao, W.; Zhou, P.; Jaroniec, M. Enhanced photocatalytic CO_2 -reduction activity of anatase TiO_2 by coexposed {001} and {101} Facets. *J. Am. Chem. Soc.* **2014**, *136*, 8839–8842. [[CrossRef](#)] [[PubMed](#)]
20. Zhang, M.M.; Zhao, K.; Xiong, J.Y.; Wei, Y.; Han, C.; Li, W.J.; Cheng, G. A 1D/2D WO_3 nanostructure coupled with a nanoparticulate CuO cocatalyst for enhancing solar-driven CO_2 photoreduction: The impact of the crystal facet. *Sustain. Energy Fuels* **2020**, *4*, 2593–2603. [[CrossRef](#)]
21. Li, S.; Wang, C.; Cai, M.; Yang, F.; Liu, Y.; Chen, J.; Zhang, P.; Li, X.; Chen, X. Facile fabrication of $\text{TaON}/\text{Bi}_2\text{MoO}_6$ core-shell S-scheme heterojunction nanofibers for boosting visible-light catalytic levofloxacin degradation and Cr(VI) reduction. *Chem. Eng. J.* **2022**, *428*, 131158. [[CrossRef](#)]
22. He, Z.; Kim, C.; Lin, L.; Jeon, T.H.; Lin, S.; Wang, X.; Choi, W. Formation of heterostructures via direct growth CN on h-BN porous nanosheets for metal-free photocatalysis. *Nano Energy* **2017**, *42*, 58–68. [[CrossRef](#)]
23. Li, Y.; Zhang, D.; Feng, X.; Xiang, Q. Enhanced photocatalytic hydrogen production activity of highly crystalline carbon nitride synthesized by hydrochloric acid treatment. *Chin. J. Catal.* **2020**, *41*, 21–30. [[CrossRef](#)]
24. Cheng, M.; Xiao, C.; Xie, Y. Photocatalytic nitrogen fixation: The role of defects in photocatalysts. *J. Mater. Chem. A* **2019**, *7*, 19616–19633. [[CrossRef](#)]
25. Ran, Y.; Yu, X.; Liu, J.; Cui, J.; Wang, J.; Wang, L.; Zhang, Y.; Xiang, X.; Ye, J. Polymeric carbon nitride with frustrated Lewis pair sites for enhanced photofixation of nitrogen. *J. Mater. Chem. A* **2020**, *8*, 13292–13298. [[CrossRef](#)]
26. He, Z.; Kim, C.; Jeon, T.H.; Choi, W. Hydrogenated heterojunction of boron nitride and titania enables the photocatalytic generation of H_2 in the absence of noble metal catalysts. *Appl. Catal. B* **2018**, *237*, 772–782. [[CrossRef](#)]
27. He, Z.L.; Que, W.X.; He, Y.C. Enhanced photocatalytic performance of sensitized mesoporous TiO_2 nanoparticles by carbon mesostructures. *RSC Adv.* **2014**, *4*, 3332–3339. [[CrossRef](#)]
28. He, Z.; Que, W.; Chen, J.; Yin, X.; He, Y.; Ren, J. Photocatalytic degradation of methyl orange over nitrogen-fluorine codoped TiO_2 nanobelts prepared by solvothermal synthesis. *ACS Appl. Mater. Inter.* **2012**, *4*, 6816–6826. [[CrossRef](#)] [[PubMed](#)]
29. Li, Y.K.; Zhang, P.; Wan, D.Y.; Xue, C.; Zhao, J.T.; Shao, G.S. Direct evidence of 2D/1D heterojunction enhancement on photocatalytic activity through assembling MoS_2 nanosheets onto super-long TiO_2 nanofibers. *Appl. Surf. Sci.* **2020**, *504*, 144361. [[CrossRef](#)]
30. Shu, Y.; Ji, J.; Zhou, M.; Liang, S.; Xie, Q.; Li, S.; Liu, B.; Deng, J.; Cao, J.; Liu, S.; et al. Selective photocatalytic oxidation of gaseous ammonia at ppb level over Pt and F modified TiO_2 . *Appl. Catal. B* **2022**, *300*, 120688. [[CrossRef](#)]
31. Wanag, A.; Kusiak-Nejman, E.; Czyżewski, A.; Moszyński, D.; Morawski, A.W. Influence of rGO and preparation method on the physicochemical and photocatalytic properties of TiO_2 /reduced graphene oxide photocatalysts. *Catalysts* **2021**, *11*, 1333. [[CrossRef](#)]
32. Diban, N.; Pacuła, A.; Kumakiri, I.; Barquín, C.; Rivero, M.J.; Urriaga, A.; Ortiz, I. TiO_2 -Zeolite metal composites for photocatalytic degradation of organic pollutants in water. *Catalysts* **2021**, *11*, 1367. [[CrossRef](#)]

33. Raditoiu, V.; Raditoiu, A.; Raduly, M.F.; Amariutei, V.; Gifu, I.C.; Anastasescu, M. Photocatalytic Behavior of Water-Based Styrene-Acrylic Coatings Containing TiO₂ Sensitized with Metal-Phthalocyanine Tetracarboxylic Acids. *Coatings* **2017**, *7*, 229. [[CrossRef](#)]
34. Bellè, U.; Pelizzari, F.; Lucotti, A.; Castiglioni, C.; Ormellese, M.; Pedefferri, M.; Diamanti, M.V. Immobilized Nano-TiO₂ Photocatalysts for the Degradation of Three Organic Dyes in Single and Multi-Dye Solutions. *Coatings* **2020**, *10*, 919. [[CrossRef](#)]
35. Yu, X.; Qiu, H.; Wang, Z.; Wang, B.; Meng, Q.; Sun, S.; Tang, Y.; Zhao, K. Constructing the Z-scheme TiO₂/Au/BiOI nanocomposite for enhanced photocatalytic nitrogen fixation. *Appl. Surf. Sci.* **2021**, *556*, 149785. [[CrossRef](#)]
36. Ding, Z.; Sun, M.; Liu, W.; Sun, W.; Meng, X.; Zheng, Y. Ultrasonically synthesized N-TiO₂/Ti₃C₂ composites: Enhancing sonophotocatalytic activity for pollutant degradation and nitrogen fixation. *Sep. Purif. Technol.* **2021**, *276*, 119287. [[CrossRef](#)]
37. Lan, K.; Wang, R.C.; Wei, Q.L.; Wang, Y.X.; Hong, A.; Feng, P.Y.; Zhao, D.Y. Stable Ti⁽³⁺⁾ defects in oriented mesoporous titania frameworks for efficient photocatalysis. *Angew. Chem. Int. Ed.* **2020**, *59*, 17676–17683. [[CrossRef](#)] [[PubMed](#)]
38. Xu, F.; Meng, K.; Cheng, B.; Wang, S.; Xu, J.; Yu, J. Unique S-scheme heterojunctions in self-assembled TiO₂/CsPbBr₃ hybrids for CO₂ photoreduction. *Nat. Commun.* **2020**, *11*, 4613. [[CrossRef](#)]
39. Shan, K.; Wang, X.; Yang, H.; Zhou, B.; Song, L.; Shang, M. Use statistical machine learning to detect nutrient thresholds in Microcystis blooms and microcystin management. *Harmful Algae* **2020**, *94*, 101807. [[CrossRef](#)] [[PubMed](#)]
40. Chen, L.; Giesy, J.P.; Adamovsky, O.; Svirčev, Z.; Meriluoto, J.; Codd, G.A.; Mijovic, B.; Shi, T.; Tuo, X.; Li, S.C.; et al. Challenges of using blooms of Microcystis spp. in animal feeds: A comprehensive review of nutritional, toxicological and microbial health evaluation. *Sci. Total Environ.* **2021**, *764*, 142319. [[CrossRef](#)] [[PubMed](#)]
41. Park, J.; Church, J.; Son, Y.; Kim, K.T.; Lee, W.H. Recent advances in ultrasonic treatment: Challenges and field applications for controlling harmful algal blooms (HABs). *Ultrason. Sonochem.* **2017**, *38*, 326–334. [[CrossRef](#)] [[PubMed](#)]
42. Oehrle, S.; Rodriguez-Matos, M.; Cartamil, M.; Zavala, C.; Rein, K.S. Toxin composition of the 2016 Microcystis aeruginosa bloom in the St. Lucie Estuary, Florida. *Toxicon* **2017**, *138*, 169–172. [[CrossRef](#)] [[PubMed](#)]
43. Sha, J.; Xiong, H.; Li, C.; Lu, Z.; Zhang, J.; Zhong, H.; Zhang, W.; Yan, B. Harmful algal blooms and their eco-environmental indication. *Chemosphere* **2021**, *274*, 129912. [[CrossRef](#)] [[PubMed](#)]
44. Li, S.; Tao, Y.; Zhan, X.-M.; Dao, G.-H.; Hu, H.Y. UV-C irradiation for harmful algal blooms control: A literature review on effectiveness, mechanisms, influencing factors and facilities. *Sci. Total Environ.* **2020**, *723*, 137986. [[CrossRef](#)] [[PubMed](#)]
45. Sun, R.; Sun, P.; Zhang, J.; Esquivel-Elizondo, S.; Wu, Y. Microorganisms-based methods for harmful algal blooms control: A review. *Bioresour. Technol.* **2018**, *248*, 12–20. [[CrossRef](#)] [[PubMed](#)]
46. Yu, X.; Jin, X.; Chen, X.; Wang, A.; Zhang, J.; Zhang, J.; Zhao, Z.; Gao, M.; Razzari, L.; Liu, H. A microorganism Bred TiO₂/Au/TiO₂ heterostructure for whispering gallery mode resonance assisted plasmonic photocatalysis. *ACS Nano* **2020**, *14*, 13876–13885. [[CrossRef](#)] [[PubMed](#)]
47. Sutthumporn, K.; Kawi, S. Promotional effect of alkaline earth over Ni-La₂O₃ catalyst for CO₂ reforming of CH₄: Role of surface oxygen species on H₂ production and carbon suppression. *Int. J. Hydrog. Energy* **2011**, *36*, 14435–14446. [[CrossRef](#)]
48. Mu, Q.; Sun, Y.; Guo, A.; Yu, X.; Xu, X.; Cai, A.; Wang, X. Bio-templated synthesis of Fe₃O₄-TiO₂ composites derived from *Chlorella pyrenoidosa* with enhanced visible-light photocatalytic performance. *Mater. Res. Express.* **2019**, *6*, 950–953. [[CrossRef](#)]
49. Liao, Y.; Qian, J.; Xie, G.; Han, Q.; Dang, W.; Wang, Y.; Lv, L.; Zhao, S.; Luo, L.; Zhang, W.; et al. 2D-layered Ti₃C₂ MXenes for promoted synthesis of NH₃ on P₂₅ photocatalysts. *Appl. Catal. B* **2020**, *273*, 119054. [[CrossRef](#)]